



Organelle-inspired supramolecular nanomedicine to precisely abolish liver tumor growth and metastasis

Jie Zhan^{a,b,c}, Yuhan Wang^d, Shaodan Ma^e, Qin Qin^b, Ling Wang^d, Yanbin Cai^{e,*},
Zhimou Yang^{b,c,d,**}

^a Shunde Hospital, Southern Medical University, The First People's Hospital of Shunde, Foshan, 528300, China

^b Guangdong Provincial Key Laboratory of New Drug Screening, School of Pharmaceutical Sciences, Southern Medical University, Guangzhou, 510515, China

^c Guangdong Provincial Key Laboratory of Construction and Detection in Tissue Engineering, Southern Medical University, Guangzhou, 510515, China

^d State Key Laboratory of Medicinal Chemical Biology, College of Life Sciences, Key Laboratory of Bioactive Materials, Ministry of Education, Collaborative Innovation Center of Chemical Science and Engineering, And National Institute of Functional Materials, Nankai University, Tianjin, 300071, China

^e Guangdong Provincial Biomedical Engineering Technology Research Center for Cardiovascular Disease, Department of Cardiology and Laboratory of Heart Center, Zhujiang Hospital, Southern Medical University, Guangzhou, 510280, China

ARTICLE INFO

Keywords:

Self-assembly
Organelle-mimicking
Nuclear delivery
Dynamic cascade process
Cancer therapy

ABSTRACT

Organelles are responsible for the efficient storage and transport of substances in living systems. A myriad of extracellular vesicles (EVs) acts as a bridge to exchange signaling molecules in cell–cell communication, and the highly dynamic tubulins and actins contribute to efficient intracellular substance transport. The inexhaustible cues of natural cargo delivery by organelles inspire researchers to explore the construction of biomimetic architectures for “smart” delivery carriers. Herein, we report a 10-hydroxycamptothecin (HCPT)-peptide conjugate **HpYss** that simulates the artificial EV-to-filament transformation process for precise liver cancer therapy. Under the sequential stimulus of extracellular alkaline phosphatase (ALP) and intracellular glutathione (GSH), **HpYss** proceeds via tandem self-assembly with a morphological transformation from nanoparticles to nanofibers. The experimental phase diagram elucidates the influence of ALP and GSH contents on the self-assembled nanostructures. In addition, the dynamic transformation of organelle-mimetic architectures that are formed by **HpYss** in HepG2 cells enables the efficient delivery of the anticancer drug **HCPT** to the nucleus, and the size–shape change from extracellular nanoparticles (50–100 nm) to intracellular nanofibers (4–9 nm) is verified to be of key importance for nuclear delivery. Nuclear targeting of **HpYss** amplifies apoptosis, thus significantly enhancing the inhibitory effect of HCPT (>10-fold) to HepG2 cells. Benefitting from the spatiotemporally controlled nanostructures, **HpYss** exhibited deep penetration, enhanced accumulation, and long-term retention in multicellular spheroid and xenograft models, potently abolishing liver tumor growth and preventing lung metastasis. We envision that our organelle-mimicking delivery strategy provides a novel paradigm for designing nanomedicine to cancer therapy.

1. Introduction

Organelles are essential constituents of cells and living systems that play important roles in the production, storage, transport, and metabolism of substances [1]. Naturally, extracellular vesicles (EVs) are responsible for the transportation of substances between cells and organs, acting as a bridge to exchange signaling molecules in cell–cell

communication [2]. Because EVs can be efficiently taken up by cells and show tissue specificity, they are used as effective drug delivery systems. For organelles inside cells, biomolecules, including proteins and RNAs, self-organize into membraneless droplets for storage and release [3]. In addition, the highly dynamic tubulin and actin filaments contribute to efficient intracellular substance transport [4], including cytoplasm-to-nucleus delivery in a treadmilling-like manner [5], in

Peer review under responsibility of KeAi Communications Co., Ltd.

* Corresponding author.

** Corresponding author. Guangdong Provincial Key Laboratory of New Drug Screening, School of Pharmaceutical Sciences, Southern Medical University, Guangzhou, 510515, China.

E-mail addresses: skyer1@smu.edu.cn (Y. Cai), yangzm@nankai.edu.cn (Z. Yang).

<https://doi.org/10.1016/j.bioactmat.2021.07.021>

Received 13 May 2021; Received in revised form 27 June 2021; Accepted 17 July 2021

Available online 24 July 2021

2452-199X/© 2021 The Authors. Publishing services by Elsevier B.V. on behalf of KeAi Communications Co. Ltd. This is an open access article under the CC

BY-NC-ND license (<http://creativecommons.org/licenses/by-nc-nd/4.0/>).

which the cargo-laden actin fibrils grow on one end and collapse on the other. Learning from these natural cues of selective substance storage and transport systems may lead to the development of efficient drug delivery carriers.

Cancer is one of the leading causes of death [6]. Although immunotherapy has recently shown substantial promise, surgery and chemotherapy remain the first choices [7]. To improve the efficacy and reduce the toxicity of chemotherapy agents, nanomedicines have been widely investigated [8–10]. However, most nanomedicines exhibit low tumor accumulation properties, particularly poor nuclear accumulation ability, thus hindering their practical applications [11]. Because the targets of many anticancer drugs are located in the cell nucleus, efficient transport from the extracellular space to the intracellular space, especially to the nucleus, is important for the development of novel nanomedicines [12]. Inspired by the highly efficient transport systems of organelles in living cells, we envision that mimicking EVs and filaments may be a fascinating strategy for developing extracellular-to-nuclear nanomedicines. However, the inherent out-of-equilibrium nature and heterogenous and crowded environments inside cells would affect the self-assembly behaviors unpredictably [13]; therefore, the design of controllable building blocks for mimetic EVs and filaments as well as actuating their spontaneous structural transformation remain challenging.

As the major structural and functional compositions in nature, proteins and peptides are involved in numerous biological processes, such as the assembly of actin proteins for cytoskeleton and cell motility and the organization of microtubules for mitosis. Owing to the advantages of peptides in bioactivity, ease of modification, and response to biological signals, self-assembling peptides have emerged as promising building blocks for the production of nanomaterials for drug delivery [14,15], bioimaging [16,17], and regenerative medicine [18,19]. Assisted by enzymes or small molecules in the cell milieu as stimuli to trigger peptide self-assembly, peptides may form self-adaptive architectures with spatiotemporal control, providing an ideal platform for creating biomimetic organelles [20,21]. Moreover, two or more successive bio-reactions in cells may confer cascade peptide self-assembly to implement precise size–shape control and efficient transportation of the resulting nanomaterials *via* pre-supposed self-assembly [22–24]. However, due to the differences of biological signals in the cell milieu, such

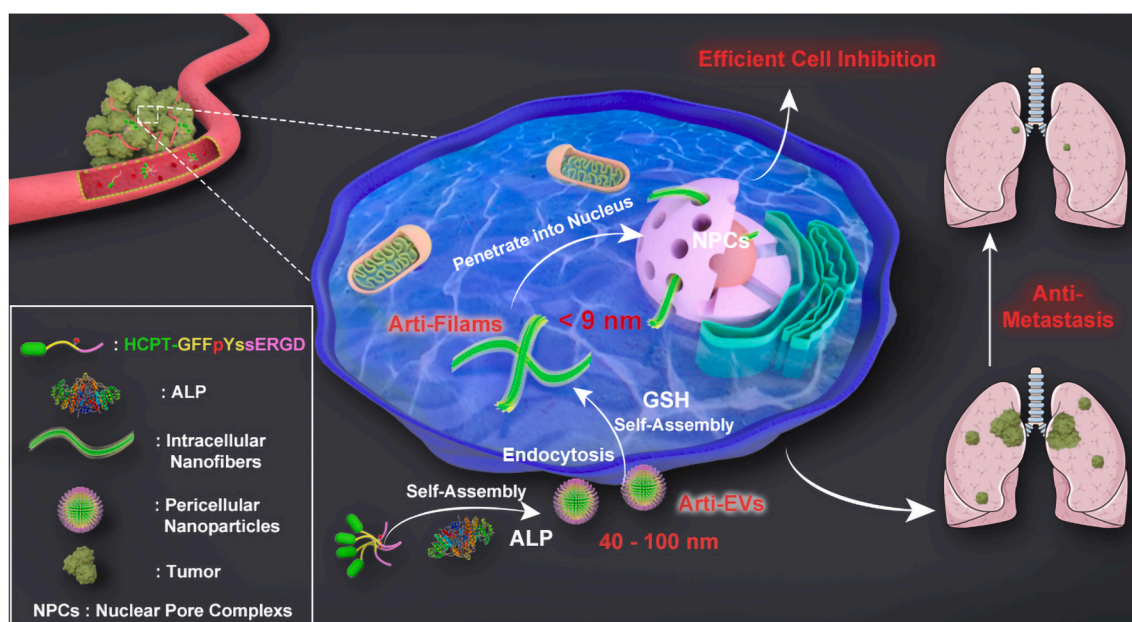
as changes in the expression level of enzymes and redox rates with gradients, the size and shape of the assemblies formed *in situ* will be affected in a manner of reaction–diffusion control in different cellular locations or different cell lines; for example, we have reported that a tandem molecular self-assembly system specifically forms pericellular nanoparticles and intracellular nanofibrils in liver cancer cells [25].

In this study, encouraged by the attractive change of self-assembly structures that arise from the stimulus of extracellular alkaline phosphatase (ALP) and intracellular glutathione (GSH) in liver cancer cells, we propose an unprecedented organelle-mimetic nanomedicine (**HpYss**) with artificial vesicles (**arti-EVs**) to artificial filaments (**arti-Filams**) transformation properties for the drug delivery (**Scheme 1**). Using an experimental phase diagram, we found that the difference in ALP and GSH content was the decisive factor that affected the resultant assemblies' morphologies. At the cellular level, ALP and GSH expressions in various cancer cell lines determine the different delivery destinations of **HpYss**. The conversion of **arti-EVs** to **arti-Filams** only occurs in HepG2 cells to deliver drugs into the nucleus by simulating the dynamic cascade process of EV-mediated membrane transport and filament-mediated nuclear transport. We speculate that the size–shape transformation from **arti-EVs** (~50–100 nm) to **arti-Filams** (4–9 nm) is of key importance for nuclear delivery. The successful nuclear-targeting enables **HpYss** to induce apoptosis; therefore, this process leads to the extraordinary inhibition of HepG2 cells. More importantly, benefitting from spatiotemporally controlled nanostructures, such artificial organelles manipulated by the multistep self-assembly process exhibit deep penetration, enhanced accumulation, and long-term retention in solid tumors depending on the self-adaptive size and shape switch *in vivo*, thus potentially abolishing liver tumor growth and inhibiting lung metastasis without damaging normal tissues.

2. Materials and methods

2.1. Preparation of organelle-mimicking nanomedicine

0.17 mg of **HpYss** was dissolved in 900 μL phosphate buffer solution (0.01 M), and then Na_2CO_3 (1 M) was added to adjust the pH to 7.4. The final volume of the solution was 1.0 mL (100 μM). The solution of **HpYss** was added with 1 U alkaline phosphatase and incubated at 37 $^\circ\text{C}$ for 12 h



Scheme 1. Schematic illustration of *in situ* sequential cellular internalization with the synergy of self-assembly kinetics and spatiotemporal size–morphology change for nucleus-targeting delivery based on an organelle-mimicking cascade delivery strategy, thereby effectively suppressing liver cancer and lung metastasis.

to trigger the first step of self-assembly to obtain **arti-EVs**. After that, GSH (400 μM) was then added to the solution for 12 h at 37 °C to trigger the second step of self-assembly and generate **arti-Filams**.

2.2. Molecule self-assembly studies in cell milieu

HepG2 cells were incubated in 6-well plate at 2×10^6 cells/well. After the cells adhered to the wall and grew for 24 h, the old culture medium was removed, washed three times, and added a new complete medium containing 100 μM of **HpYss**. Then the medium was collected at 0.5 h to perform TEM imaging for observing the **arti-EVs** formed by the first-step self-assembly in the pericellular space. After 2 h incubation, the medium mixed with **HpYss** was removed, cells were washed with PBS for three times, digested with trypsin, centrifugated at 1000 rpm, and then fixed by 2.5 % glutaraldehyde at 4 °C for bio-TEM imaging to survey the **arti-Filams** formed by the second-step self-assembly in the cells.

2.3. Bio-TEM experiment for ultrathin sections of cells

The **HpYss** treated HepG2 cells fixed by 2.5 % glutaraldehyde were washed three times with PBS and fixed in the buffer (Dalton's osmium in potassium dichromate) for 2 h, then the cells were rinsed triple in PBS. After that, the samples were dehydrated through acetone solutions with the increasing concentrations (50 %, 70 %, 80 %, 96 %, three times of 100 %, 10 min each time), and propylene oxide Epon 812 mixture for twice (1:1 and 1:2, respectively). Finally, the samples were infiltrated with pure Epon 812 overnight at 4 °C, then solidified for 24 h at 37 °C, 45 °C, 60 °C, respectively. Before the samples were observed by TEM, they were sectioned transversely or longitudinally with a thickness of 80 nm, put onto copper grids, negative-stained with 2 % uranyl acetate for 0.5 h, incubated in 3% lead citrate for another 10 min, and rinsed with H_2O .

2.4. Sequential cellular internalization and intracellular distribution

All the cell lines were incubated in glass-bottom cell culture dishes at a density of 1×10^5 cells per dish. After incubation for 24 h, complete medium containing 100 μM of different compounds was added to the dishes. Next, the medium was removed at 0.5, 2, and 4 h, and the cells were washed with PBS three times. The cells were incubated with $1 \times \text{Reddot}^{\text{TM}}$ (Biotium, 40060–1) for 20 min at 37 °C in the dark to stain nuclei and kept in the live cell imaging solution before observation under a microscope. In the competitive-binding experiments, HepG2 cells were incubated with 10-fold molar excess of c (RGDFc) (1 mM) for 1 h prior to the addition of 100 μM **HpYss**. Images were recorded using a confocal laser scanning microscope (Leica TSC SP8) at the same voltage. ($\lambda_{\text{exc.}} = 405 \text{ nm}$ for the green (HCPT) channel, $\lambda_{\text{exc.}} = 633 \text{ nm}$ for red (nucleus) channel). The fluorescence intensity quantified from the grayscale value was obtained using ImageJ.

2.5. Cell apoptosis analysis

To access apoptosis on HepG2 cells treated with different formulations, the fluorescence-activated cell sorting (FACS) was carried on by an Annexin V-Alexa Fluor 647/PI double-staining assay. First, 5×10^5 cells/well of HepG2 cells were seeded in 6-well plates and incubated for 24 h. Then, 200 nM of **HpYss**, **HYss**, **HYs**, **HpYG**, free HCPT, and drug-free culture medium were added to each well. After 48 h incubation at 37 °C, the cells were harvested, centrifuged, washed, resuspended in binding buffer, and stained with Annexin V-Alexa Fluor 647/propidium iodide (PI). The numbers of early apoptotic (positive for Annexin V-Alexa Fluor 647), apoptotic (double-positive for Annexin V-Alexa Fluor 647 and PI), and necrotic (positive for PI) cells were determined by a CytoFLEX S flow cytometer (Beckman Coulter, USA).

2.6. Multicellular spheroids (MCSs) studies

After the HepG2 3D MCSs were successfully constructed (see supplementary materials), the MCSs were incubated with 100 μM of different formulations. Six hours later, the MCSs were collected and centrifuged, washed with PBS, and then added to a confocal dish for imaging ($\lambda_{\text{exc.}} = 405 \text{ nm}$ for the green channel). In the MCS inhibition experiments, the MCSs were incubated with 100 μM of different formulations and the medium was replaced every two days. The spheroid volume was calculated using the following formula:

$$V = \frac{4}{3}\pi r^3$$

where r is the radius of the spheroid.

2.7. In vivo fluorescence imaging

Animal experiments were performed in accordance with the guide for the care and use of laboratory animals published by the US National Institutes of Health (8th edition, 2011) and approved by the Institutional Animal Care and Use Committee (IACUC) of Southern Medical University, China. Female BALB/c nude mice (4–6 weeks, 16–19 g) were purchased from Guangdong Medical Laboratory Animal Center, China. HepG2 cells (1×10^7) were subcutaneously implanted into these mice on the right hind limb. The tumor volume was calculated using the following formula: length \times width²/2. When the tumor size reached 30 mm^3 , the mice were randomly grouped four (five mice per group). The four groups of mice were injected with **cy-HpYss**, **cy-HYss**, **cy-HYs**, **cy-HpYG** (drug dose: 3 mg/kg HCPT-equivalent dose, Table S1) through the tail vein. The mice were then imaged using the IVIS Lumina II system at 4, 8, 12, 24, and 60 h post-injection. Further, tumors and other main organs (heart, liver, spleen, lung, and kidney) were harvested for *ex vivo* imaging at 24 h post-injection. and imaged at the end of the experiment. The fluorescence of the main organs was calculated using the IVIS Lumina II system.

2.8. Pharmacokinetics and biodistribution

To evaluate the pharmacokinetics of different formulations, female BALB/C mice were randomly divided into five groups (five mice per group), and administrated intravenously with **HpYss**, **HYss**, **HYs**, **HpYG**, and free HCPT at a dose of equivalent to 3 mg HCPT/kg, respectively. Approximately 500 μL of blood samples was collected by eyeball extirpation within a heparinized capillary tube at 0.25, 0.5, 1, 2, 4, 6, 24 h post-injection, and centrifuged at $2500 \times g$ for 15 min to harvest plasma samples. Then the samples were suspended in DMSO to extract the drugs, subsequently centrifuged at $9800 \times g$ for 10 min to obtain the supernatant. The content of HCPT in supernatant was then examined by liquid chromatography-mass spectrometry (Shimadzu LCMS-20AD). Pharmacokinetic parameters such as $\tau_{1/2\beta}$, CL, Vd, and AUC were calculated by fitting the blood drug pharmaceutical concentrations in a two-compartment model using EXCEL software. For assessment of tissue distribution, the HepG2 tumor-bearing nude mice were intravenously injected with **HpYss**, **HYss**, **HYs**, **HpYG**, and free HCPT at a dose of equivalent to 3 mg HCPT/kg, respectively. The heart, liver, spleen, lung, kidney, and tumor tissues were harvested from the sacrificed mice at 1, 6, 24 h post-injection, respectively. The excised organs were washed with saline, weighed after drying, and homogenized in 0.5 mL DMSO, followed by centrifugation at $9800 \times g$ for 10 min. The content of HCPT inside each tissue was detected by liquid chromatography-mass spectrometry. The following equations were used to calculate the percent injected dose (%ID) and the percent ID per gram (%ID/g) values:

$$\%ID = \frac{\text{dose in plasma/tissue sample}}{\text{injected dose}} \times 100$$

$$\%ID / g = \frac{\%ID}{\text{weight of tissue (g)}} \times 100$$

2.9. In vivo antitumor efficacy

All HepG2 xenografts mice were constructed as described above. When the tumor size reached 60 mm³, the mice were randomly divided into six groups (five mice per group) and i. v. administrated with **HpYss**, **HYss**, **HYs**, **HpYG**, free HCPT, and saline (drug dose: 3 mg/kg HCPT-equivalent dose, Table S2). The day of first dosing was designated as day 0, and all the formulations were injected once every three days with the termination of injection after 9 days. Tumor size and body weight were monitored once every three days for 30 days. A similar method was employed for the treatment of mice in a large-tumor model with the initial tumor volume of 300 mm³, except that the administration was performed four times.

2.10. Histopathological examination

Major organs of the mice, including the heart, liver, spleen, lung, kidney, and tumor, were harvested and collected immediately after the inhibition experiment for H&E histological analysis and immunofluorescence. The tissues were fixed in 4 % paraformaldehyde and embedded in paraffin after dehydration with gradient ethanol. After that, the tissues were cut into slices at a thickness of 5 μm and then deparaffinized with xylene and gradient ethanol. The tissues were stained with hematoxylin and eosin to assess histological alterations, or the TUNEL kit (DeadEnd™ Fluorometric TUNEL System, Promega, G3250), Ki67 (Abcam, ab16667), and CD31 (Abcam, ab28364) for immunofluorescence analysis, and eventually visualized using a confocal microscope (Leica TSC SP8). The fluorescence intensity of images by confocal laser scanning microscopy was calculated using Image J.

2.11. Hematological toxicities

We divided normal Balb/c nude mice (4–6 weeks, 16–19 g) into six groups (five mice per group) and treated them with **HpYss**, **HYss**, **HYs**, **HpYG**, free HCPT, and saline (dose: Table S2) three times. We designated the first day after three administrations as D1 and the fifth day as D5. Whole blood samples were collected from the eyes on D1 and D5. Blood samples (300 μL) were collected into heparinized tubes for hematological analysis. The blood sample (500 μL) was harvested into a heparinized capillary tube, and the supernatant was collected after centrifugation at 2500×g for 15 min to conduct biochemical analysis.

2.12. Lung metastases model

For the lung metastasis model of the liver cancer cells, 1 × 10⁶ HepG2-luci cells in 200 μL serum-free DMEM culture medium were injected into Balb/c nude mice by tail vein (4–6 weeks, 20 ± 2 g). After inoculation at day 6 (designated as day 0), all mice were randomly divided into six groups (five mice per group) and administrated intravenously with **HpYss**, **HYss**, **HYs**, **HpYG**, free HCPT, and saline with drug dose equivalent to 3 mg/kg HCPT. Four injections were performed at 2 days intervals (0, 3, 6, 9 day), and the experiments were terminated at day 30. The liver cancer cells retention and invasion in the lung were monitored using the bioluminescence signal of the HepG2-luci cells by the IVIS imaging system (HCPT does not interfere with the bioluminescence imaging). Then the mice were euthanized; the lungs were extracted and rinsed with PBS, followed by adding 100 mL of Bouin's fixative solution (Solarbio G2331) for preservation of the original morphology of cells and tissues. 24 h after fixation, optical photos were taken for further observation. Furthermore, the excised lung tissues were fixed with 10 % formalin to prepare paraffin sections and stained with

H&E to evaluate the area of lung damage.

2.13. Statistical analysis

All experiments were performed in more than three specimens. Data were presented as means ± standard deviation. Statistical analysis was performed using GraphPad Prism 5 and SPSS (Statistical Package for the Social Sciences) version 22.0. A one-way ANOVA test of multiple comparisons followed by Dunnett's post-hoc test was used to determine statistical significance of the data. The differences were considered significant for p values * <0.05, ** <0.01, *** <0.001.

3. Results and discussion

3.1. Molecular design and self-assembly behavior of organelle-mimicking nanomedicine

The organelle-mimicking nanomedicine is initiated from a drug-peptide conjugated precursor (**HpYss**) comprising two parts: one is the anticancer drug (HCPT), and the other is the cascade-activatable peptide motif GFFpY-ss-ERGD integrating the L-phosphotyrosine (pY) and the disulfide linker (ss) to trigger ALP-instructed self-assembly and thiol-responsive self-assembly, respectively (Fig. 1A and Scheme S1) [26,27]. The control compounds as follows were also synthesized: **HYss** (lack of phosphate), **HYs** (lack of phosphate, disulfide, and ERGD motif), and **HpYG** (lack of disulfide) (Scheme S2). In consideration of the actin filaments at a concentration of 100 μM in cells, we chose this concentration to study the sequential self-assembly behaviors of **HpYss** [28]. After the addition of ALP (1 U/mL) to the solution of **HpYss** (PBS, pH = 7.4), approximately 70 % of **HpYss** was converted to **HYss** within 90 min, and then more than 75 % of **HYss** could be converted to **HYs** in the presence of GSH (400 μM) after 14 h (Fig. S1). The size and morphology of the corresponding nanostructures were characterized by transmission electron (TEM) and atomic force (AFM) microscopies. The results in Fig. S2 showed that the dephosphorylated **HYss** self-assembled into uniform nanoparticles (50–100 nm) with appropriate diameters to act as **arti-EVs**, and the self-assembly of **HYs** obtained nanofibers (4–9 nm) with a fine-matched size that were ideal candidates for **arti-Filams** [29].

The optical images showed the self-assembly induced by ALP and GSH extended the micellar stability of **HpYss** to more than a week, and the gradually stronger laser beam in the solution of **HYss** and **HYs** indicated more intensive assemblies existed (Fig. S3). Accordingly, the calculated critical aggregate concentration (CAC) values of **HYss** (64.2 μM) and **HYs** (23.4 μM) were lower than **HpYss** (91.7 μM) due to the disconnection of hydrophilic phosphate and amino acids (Fig. S4). However, due to the supramolecular nature of self-assembly, the architectures of the obtained assembly-entities were complex, whereas the hydrophilic-hydrophobic balance was hypothesized to be the core factor managing the assembly behavior. Therefore, the content of ALP and GSH (A&G) as a variable parameter was introduced to systematically investigate the transition of self-assembled morphology. On the basis of an experimental assembly library of the responsive nanostructures of **HpYss** under a range of A&G contents, we proposed a rough phase diagram dependent on TEM images. As shown in Fig. 1B and Fig. S5, **HpYss** could form irregular oligomers spontaneously, and it maintained the structure of small aggregates at a relatively low A&G content. The nanoparticles mainly appeared under the condition of high ALP concentration with low GSH concentration. When the GSH concentration increased to 200 μM, nanofibers emerged and coexisted with nanoparticles in the system. Once the concentration of GSH rose to 400 μM, the nanostructures were completely fibrous in a wide range of ALP concentrations. As the GSH increased gradually, the precipitation would appear in the system, and the compounds thoroughly precipitated under the stimuli of 1000 μM GSH. Table S3 displayed the size of nanostructures in Fig. S5.

The change of molecular arrangement driven by the alteration of the

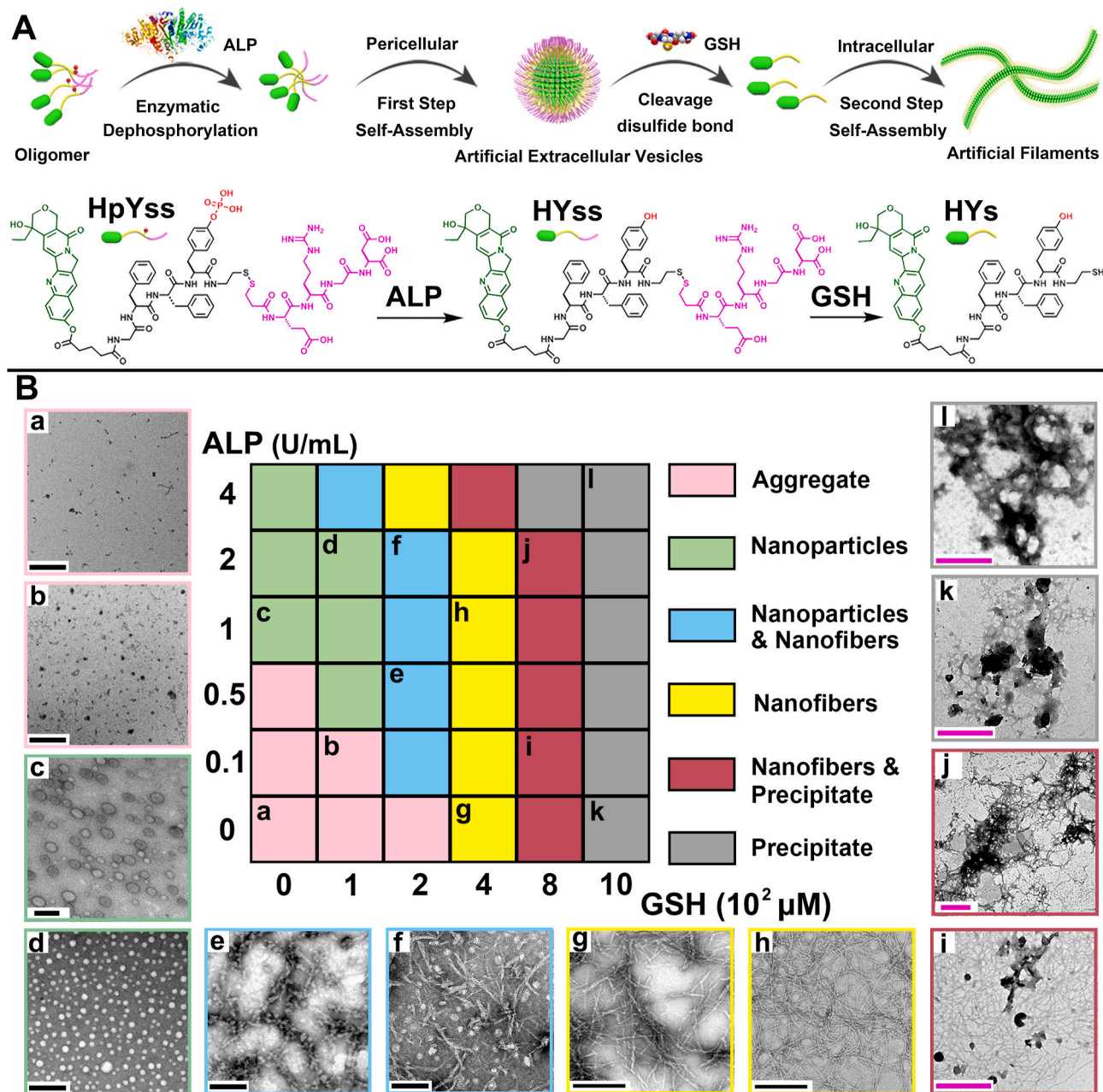


Fig. 1. Illustration and characterization of organelle-mimicking nanomedicine. (A) Molecular design and sequential conversion steps to form **arti-EVs** and **arti-Filaments** through molecular self-assembly with triggering by ALP (1 U/mL) and GSH (400 μM). (B) Phase diagram of the nanostructures of **HpYss** (100 μM) after sequential stimulation by ALP and GSH in different contents (black scale bar: 200 nm; pink scale bar: 500 nm).

hydrophilic–hydrophobic balance is most likely the inherent reason for generating rich and diverse nanostructures. Circular dichroism (CD) was used to assess the superstructures of self-assembled entities. As shown in Fig. S6, a negative peak at 195 nm and a broad negative peak at 212–225 nm were observed in the CD spectra of the dephosphorylated **HYss**, and the analysis result indicated that a mixed conformation contained certain proportions of α -helix, β -sheets, and unordered coil patterns. In contrast, the **HYs** resulted from the further disulfide cleavage exhibited a typical “cotton effect” absorption with a positive peak at 194 nm and a negative peak at 210 nm, indicative of the formation of a highly ordered β -sheet-rich structure [30]. We inferred that although the hydrophilicity of molecules was decreased by the disconnection of phosphate, peptide chains were not changed and, therefore, retained the feature of flexibility to form sphered nanostructures with a more curved interface. However, the hydrophilic segments of peptide chains were

reduced by the GSH triggering that rendered the remaining aromatic peptide motif inclined to form nanofibers with β -sheets configurations. When the hydrophilic segments were rapidly removed by high GSH concentrations, the hydrophobicity of molecules instantaneously increased, and the precipitates formed. Collectively, the variation of A&G contents dictated the morphologies of assembled nanostructures, which would eventually affect the composition of an organelle-mimicking nanomedicine.

3.2. Organelle-mimetic cellular internalization and nuclear delivery

The designed organelle-mimicking nanomedicine would exhibit different delivery efficiencies due to the variable composition of **arti-EVs** and **arti-Filaments** governed by the distinguishing ALP and GSH contents in different cell lines. We monitored the cell internalization by

confocal laser scanning microscopy (CLSM) in six cell lines (cancerous: HeLa, MCF-7, A549, and PC-3 cells; noncancerous: LO2 cells). As shown in Fig. 2A, after incubation with the precursor of organelle-mimicking nanomedicine (HpYss) for 4 h, we surprisingly observed that the green fluorescence from HCPT accumulated in the nucleus of HepG2 cells and colocalized well with the red fluorescence of the nuclear dye; however, the green fluorescent signals were only tracked in the cytoplasm of the other five cell lines. The corrected total cell fluorescence quantification of HpYss showed that the statistical values in cancer cells were higher than normal cells (LO2). Because HpYss only reached the deepest destination in HepG2 cells (i.e., it delivered the drugs into the nucleus), it had the highest statistical fluorescence intensity within cells (Fig. S7). With reference to the experimental and reported results (Fig. S8) [25,31,32], we found that HepG2 cells expressed both high

contents of ALP and GSH, which might be the key factor of the nuclear internalization of HpYss.

To confirm this point, we insightfully investigated the delivery process of HpYss in HepG2 cells. As shown in Fig. S9, after incubation with HpYss for 0.5 h, the green fluorescence puncta were observed on the surface of HepG2 cells; then, the green fluorescent coverage increased and migrated from outside the cell into the cytoplasm and reached the nucleus at 4 h, indicating the sequential cell internalization for cascade nuclear delivery. The bio-TEM was utilized to explore the extra- and intra-cellular microscopic morphology of HpYss in HepG2 cells. After coculturing the cells with 100 μM of HpYss for 0.5 h, we observed well-defined nanoparticles with diameters of 50–100 nm from the collected culture medium, demonstrating the local formation of arti-EVs outside the cells (Fig. 2B). In contrast, similar nanoparticles could not be

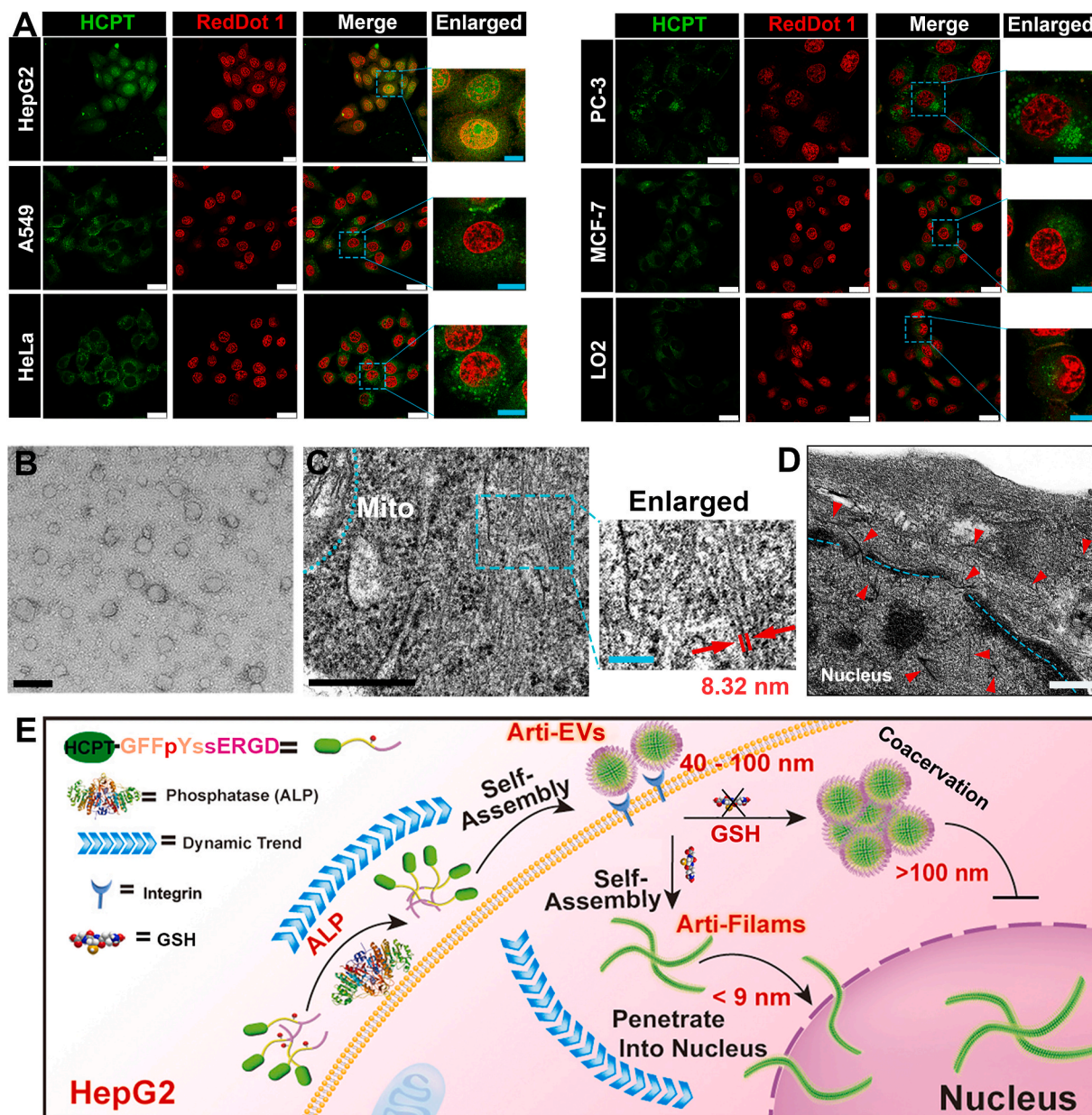


Fig. 2. Organelle-mimicking nanomedicine in cell milieu and sequentially cellular internalization for membrane-to-nucleus delivery. (A) CLSM images of different cell lines treated with 100 μM of HpYss for 4 h (white scale bar = 25 μm, cyan scale bar = 10 μm, λ_{exc} = 405 nm for the green channel, and λ_{exc} = 633 nm for the red channel). (B) TEM image of collected culture medium from HepG2 cells incubated with HpYss (100 μM) for 0.5 h; scale bar: 200 nm. (C) Bio-TEM image of HepG2 cells incubated with HpYss (100 μM) for 2 h; cyan dashed line represents the mitochondrion boundary; black scale bar: 500 nm, cyan scale bar: 100 nm. (D) Nanofibers crossing the nuclear pore into the nucleus observed by the bio-TEM image of HepG2 cells; red triangles mark the nanofibers extra and intra nucleus; scale bar: 200 nm. (E) Schematic illustration of proposed self-adaptive membrane-to-nucleus delivery by the organelle-mimicking cascade process.

observed when HepG2 cells were pretreated with the ALP activity inhibitor (DQB), which verified the nanostructures existed in Fig. 2B were not the endogenous extracellular vesicles (Fig. S10) [33]. As the incubation time increased to 2 h, filaments with diameters of approximately 7 ± 2 nm were clearly found inside the cells (Fig. 2C). When we used L-buthionine-sulfoximine (BSO, an inhibitor of γ -glutamylcysteine synthetase, to decrease GSH levels) [34] to pretreat the cells for 2 h, no similar fibrous morphology was observed in the cells (Fig. S11). Consequently, the intracellular thiol-induced self-assembly contributed to the formation of **arti-Films**. Combined with the above results, we speculated that the time-dependent growth of green fluorescence and the location changes represented the spatiotemporally migrated feature of **HpYss**, which simulated a relay process of EV-mediated membrane delivery to filament-mediated nuclear delivery.

Because the EVs' entry into cells was underpinned by well-defined endocytosis mechanisms [35], identifying the uptake routes of **HpYss** would be a valid method to analyze the dynamic relay process of organelle-mimicking drug delivery. The RGD motif in **HpYss** had high affinity for $\alpha v \beta 3$ integrins overexpressed on cancer cells, indicated it would undergo receptor-mediated binding and endocytosis. This process was demonstrated by the CLSM images, in which negligible green fluorescence was observed in HepG2 cells pre-treated with excess inhibitor of $\alpha v \beta 3$ (c (RGDFC)) to competitively block integrin receptors binding (Fig. S12) [36]. Subsequently, the internalization mechanism of **HpYss** was investigated by some known inhibitors of endocytosis. We found that the cellular uptake of **HpYss** was completely inhibited by the marker of clathrin-mediated endocytosis (CPZ) and a certain extent inhibited by the marker of caveolae/lipid raft-mediated endocytosis (Filipin III), illustrating that **HpYss** crossed the cell membrane via these two forms of endocytosis rather than the passive diffusion that small molecules went through (Fig. S13) [37]. These results demonstrated that **HpYss** firstly formed **arti-EVs** (namely biomacromolecules) by extracellular self-assembly before moving into cells.

Subsequently, **HpYG** without the GSH-responsive site was used to study the role of intracellular self-assembly for organelle-mimicking nuclear internalization. As expected, CLSM images in Fig. S14 showed that the green fluorescence remained in the cytoplasm after the HepG2 cells had been incubated with **HpYG** for 4 h. In addition, when the intracellular GSH was depleted by pretreating HepG2 cells with BSO for 2 h, the green fluorescence of **HpYss** also disappeared in the nucleus (Fig. S15). These observations indicated that **arti-Filams** formed by intracellular self-assembly might be crucial for nuclear trafficking. Unexpectedly, when the prefabricated **arti-EVs** (**HYss**) and **arti-Filams** (**HYs**) were incubated with HepG2 cells for 4 h, their green fluorescence exhibited bright fluorescent droplets outside the nucleus rather than reaching the nucleus (Fig. S14). The bio-TEM images of HepG2 cells treated with **HpYss** for 4 h displayed obvious nanofibers surrounding the nucleus and passing through the nuclear pores into the interior (Fig. 2D); however, when the cells were treated with **HYss**, the small vesicles coalesced into larger particles in the cytoplasm, which was similar to a phase transition process known to locally concentrate proteins (Fig. S16). Moreover, the mean fluorescence intensity (MFI) detected by flow cytometry and manifesting the quantity of **HpYss** was approximately 3-fold higher than that of **HYss**, **HYs**, and **HpYG**, and 20-fold higher than that of free HCPT in the cytoplasm (Fig. S17). Meanwhile, the calculated fluorescence accumulated in the nucleoplasm from the extracted nuclei showed that the **HpYss** group was substantially higher than other groups (nearly 10-fold higher, Fig. S18). Collectively, these results demonstrated that the single step of intracellular self-assembly by **arti-EVs** or the nanostructures equivalent to **arti-Filams** could not implement nuclear internalization in HepG2 cells.

The size and shape of nanomedicines are key factors for their entry into the nucleus, and exogenous nanoparticles with diameters <9 nm can enter the nucleus freely [38,39]. In addition, the high aspect ratio of rods (5–10 nm \times 100–300 nm) and worms (5–10 nm \times 400–700 nm) diffuse into the nucleus more easily than low-aspect-ratio spherical

nanoparticles [40,41]. Combining with the *in situ* self-assembled **arti-EVs** and **arti-Filams** from **HpYss** in HepG2 cells, it is tempting to speculate that the organelle-mimicking drug delivery could achieve the most appropriate conditions of nuclear trafficking through the spatiotemporal size and shape transformation. However, in the absence of dynamic tandem self-assembly for the membrane-to-nucleus process, the protein-like assemblies are inclined to a liquid-liquid phase transition to form liquid droplets, which enlarge the nanostructures to prevent nuclear transport (Fig. 2E).

3.3. *In vitro* anticancer effects

Benefitting from organelle-mimicking nuclear-targeted delivery, **HpYss** exhibited the highest *in vitro* cytotoxicity to HepG2 cells with a half-maximum inhibition concentration (IC_{50}) as low as 80 nM, which was approximately 4–5-fold lower than that of **HYss** (355 nM), **HYs** (423 nM), **HpYG** (439 nM), and 10-fold lower than that of free HCPT (840 nM), indicating the outstanding capacity of **HpYss** to kill HepG2 cells (Fig. 3A and Fig. S19). We then utilized fluorescence-activated cell sorting (FACS) to determine the apoptosis induced by different formulations. There was no significant difference in the percentage of apoptosis between cells treated with **HYss**, **HYs**, and **HpYG**, with a total apoptosis rate of approximately 30 % (200 nM, 48 h). The proportion of apoptotic and necrotic cells incubated with **HpYss** increased significantly to 13.6 % (early apoptotic), 75.3 % (late apoptotic), and 2.44 % (necrosis), confirming that the largest extent of apoptosis of HepG2 cells was induced by the treatment with **HpYss** (Fig. 3B and C). The cytotoxicity evaluation in different cell lines showed that, comparatively, the IC_{50} of free HCPT was 10-fold higher than that of **HpYss** in HepG2 cells, whereas it was 3.70-fold higher in MCF-7 cells, 4.21-fold higher in HeLa cells, and less than one-fold higher in PC-3 cells and A549 cells (Fig. 3D and Fig. S20). The IC_{50} of **HpYss** was significantly lower than that of free HCPT in noncancerous LO2 cells, indicating the lower toxicity of **HpYss** to normal cells. These results demonstrate the remarkable inhibition capacity of **HpYss** in liver cancer, most likely due to the organelle-mimicking nuclear-targeting delivery.

3.4. Penetration and inhibition of tumor spheroids

The size and shape of a particular nanomedicine are inherently conflicting attributes for improving delivery efficiency in cancer treatment [42]. Small molecules with reduced diffusional hindrance show increased tumor penetration but inferior tumor accumulation. Large nanoparticles preferentially accumulate in solid tumors but endure high interstitial transport pressure to penetrate the tumor's interior [43]. The tunable size and shape from **arti-EVs** to **arti-Filams** encouraged us to explore the advantage of **HpYss** in tumor penetration and improved therapeutic efficacy (Fig. 4A). We first studied the inhibitory efficacy of **HpYss** against HepG2 3D multicellular spheroids (MCSs). As shown in Fig. 4B, MCSs in the control group continued to grow throughout the study period, reaching 160 % of the initial volume after 7 days (Fig. 4C). Compared to the stable volume of MCSs treated with free HCPT, the volume in **HYss**, **HYs**, and **HpYG** groups exhibited a moderate decrease to ~50% of the primary size, indicating that the integration of peptide motifs with HCPT could improve its inhibitory effects on solid tumor spheroids. Notably, the MCSs co-incubated with **HpYss** showed the best performance in growth inhibition, with a reduced MCS volume to 20 % of the prime (Fig. 4B and C). We then employed CLSM to confirm the penetrability of the different formulations in HepG2 MCSs. Fig. 4D shows that **HpYss** and **HpYG** reached the interior of MCSs with a steady intensity (100 μ m depth), whereas the green fluorescence signals of **HYss** and **HYs** were in the peripheral region of the MCS at the same scale. The 3D pattern of the tumor spheroids in Fig. 4E reflected the **HYss** and **HYs** covering the periphery of the spheroid with a maximum depth of approximately 50 μ m, whereas **HpYss** and **HpYG** were distributed over the entire spheroid at depths of 100 μ m. These results

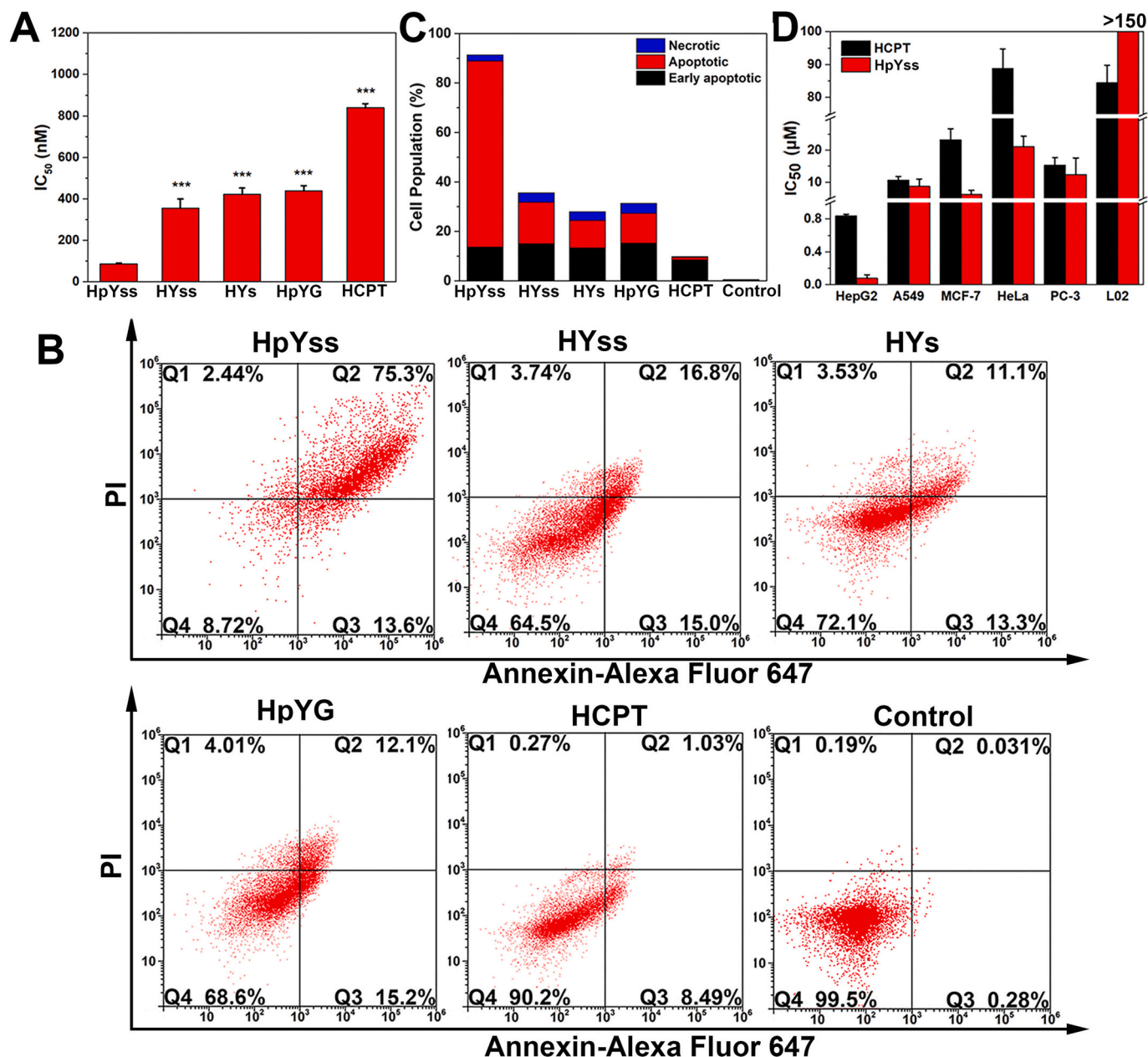


Fig. 3. *In vitro* cytotoxicity and apoptosis evaluation. (A) IC₅₀ values of HepG2 cells incubated with different formulations for 48 h. (B) Annexin V-Alexa Fluor 647/PI staining assays of HepG2 cells after incubation with 200 nM of different formulations for 48 h. (C) Population of early apoptosis, apoptosis, and necrosis in HepG2 cells from (B). (D) IC₅₀ values of different cell lines incubated with HpYss for 48 h. Data are presented as mean ± SD, N = 3, ***P < 0.001 vs. HpYss group.

demonstrated that the precursors of assemblies with small size might possess a better permeability to tumors, which was probably because of their convective transport. For the assemblies, it is not clear whether prefabricated nanoparticles (arti-EVs) or nanofibers (arti-Filams) would exhibit limited penetrability because of their relatively bulky size (although for a single fiber of 3–8 nm, the intertwined fibers form cluster structures to hinder their extravasation).

3.5. *In vivo* biodistribution and *in situ* accumulation in tumors

The pharmacokinetics and biodistribution of different formulations in HepG2-bearing female nude mice were investigated. A higher initial concentration (equal to 3 mg/kg HCPT, > 1 mM) of different formulations with slightly negative or nearly neutral charges was used to overcome the rapid degradation and non-specific uptake in blood circulation (Fig. S21) [44]. The concentration-time profiles and the

calculated pharmacokinetic parameters in Fig. S22 showed that the elimination half-life ($t_{1/2}$) of the four drug-peptide conjugates was prolonged within a narrower range than that of free HCPT (<2-fold), whereas the prefabricated arti-EVs (HYss) and arti-Filams (HYs) exhibited a slightly longer retention time attributed to the nanostructures. Interestingly, the smaller total volume distribution (V_d) values of HpYss and HpYG implied that they might have a better targeting potential. The biodistribution results confirmed the higher accumulation of HpYss and HpYG than other groups at the tumor site by quantitative analysis of extracted tumors. In particular, the accumulated HpYss in tumors was 13.6-fold higher than that in the free HCPT at 24 h; simultaneously, the amount of HpYss accumulated in normal tissues remarkably decreased to the lowest level in all groups (Fig. S23).

Except for the study above, in which structural alteration facilitated tumor penetration, our recent work and lots of relative studies from other researchers also demonstrated that the nanostructures formed *in*

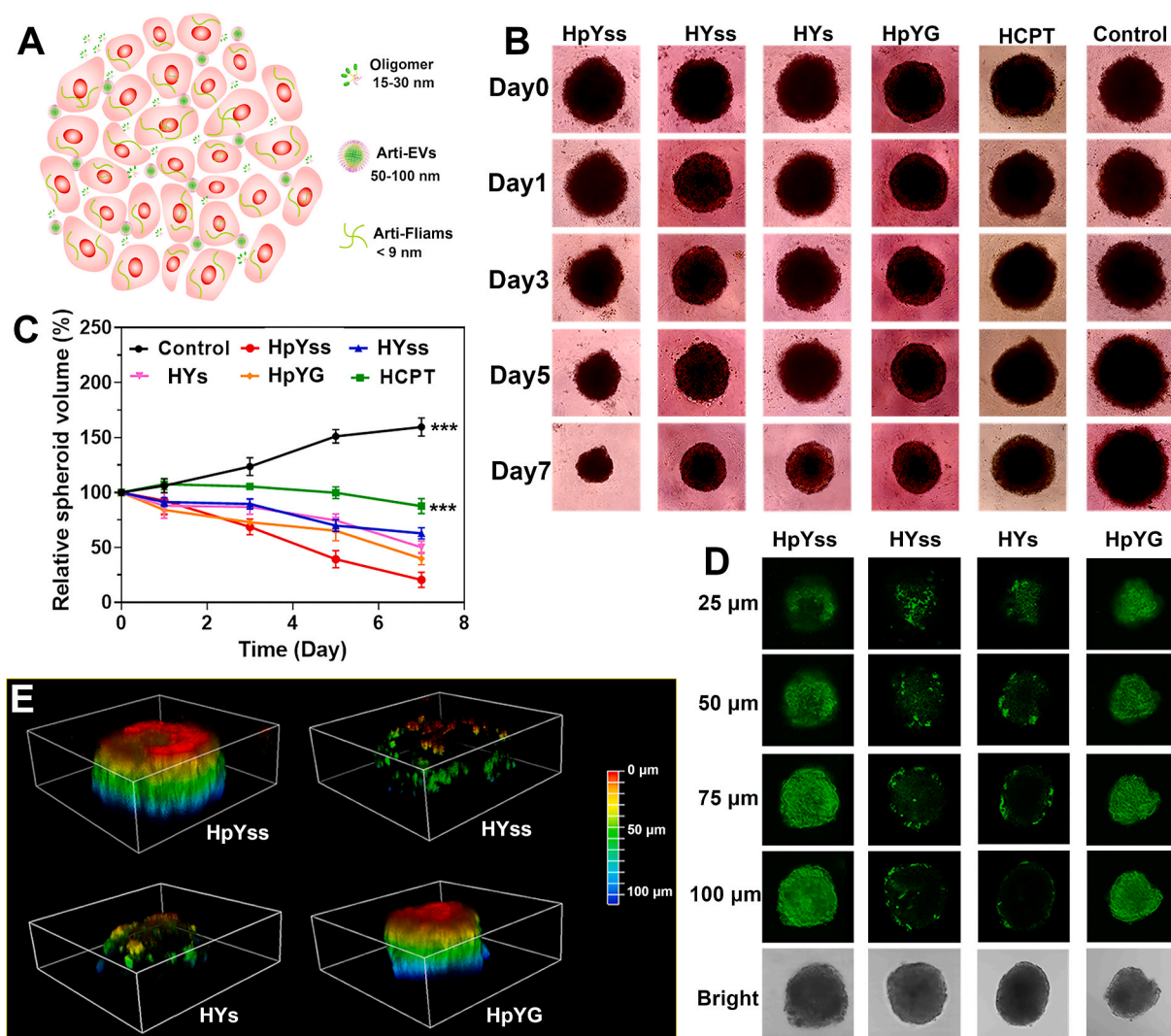


Fig. 4. Organelle-mimicking nanomedicine improves the therapeutic potency and penetration in tumor spheroids. (A) Schematic illustration of the advantage of *in-situ* self-assembly in tumor penetration. (B) Evaluating the inhibition of HepG2 3D MCSs' growth by treating spheroids with 100 μ M of different formulations; spheroids were treated with drug-free culture medium as the control. (C) Volume of HepG2 MCSs in different groups at various time points compared to their respective volumes at day 0. (D) CLSM images of HepG2 MCSs incubated with 100 μ M of HpYss, HYss, HYS, and HpYG for 6 h; scale bar: 100 μ m. (E) CLSM images in a 3D pattern for HepG2 MCSs of (C). Data are presented as mean \pm SD, N = 3, *** P < 0.001 vs. HpYss group.

situ by small molecular peptides crossing the blood vasculature and penetrating the tumor site could accumulate within the tumors *in vivo* through an assembly-induced retention (AIR) effect [45,46]. Thus, we reasonably inferred that the *in situ* formation from **arti-EVs** to **arti-Filams** was advantageous for drug accumulation and retention in tumors *in vivo* (illustrated in Fig. 5A). Bio-TEM results provided evidence of abundant fibrous structures in tumor tissues after the administration of HpYss, in which the dense filaments were identified at the site adjacent to the nucleus of tumor cells (Fig. 5B). Moreover, cyanine5.5-labeled formulations were utilized to further verify this inference (Cy-HpYss, Cy-HYss, Cy-HYS, and Cy-HpYG, Scheme S2). Under the sequential triggering of ALP and GSH to induce Cy-HpYss self-assembly, the corresponding nanoparticles (**arti-EVs**) and nanofibers (**arti-Filams**) were also observed in the TEM images (Fig. S24). By employing xenograft HepG2 tumor-bearing mice, we intravenously injected the four probes with the concentration equal to 3 mg/kg HCPT (>1 mM) for imaging using the *In Vivo* Imaging System (IVIS). Cy-HpYss exhibited a concentrated accumulation in the tumor site at 24 h, and the signal persisted for up to 60 h. However, the fluorescence signal of Cy-HYss and Cy-HYS in the tumor site weakened gradually and even disappeared

at 24 h after injection, potentially due to their limited penetrability (Fig. 5C). Although Cy-HpYG exhibited an equivalent permeability to Cy-HpYss, its retention effect at the tumor site was still defective owing to the lack of the second-step self-assembly to form **arti-Filams**. The main organs and tumors were harvested to further evaluate the distribution of different formulations *ex vivo* (60 h post-injection of Cy-HpYss and 24 h post-injection of other formulations, Fig. 5D), in which the quantitative value of fluorescence signals demonstrated that Cy-HpYss at the tumor site at 60 h was much higher than that of other formulations at 24 h (Fig. S25). In addition, *ex vivo* imaging showed strong fluorescence signals in the kidney, indicating that all of these peptide derivatives were removed from the body mainly by renal clearance [47]. These results suggested that organelle-mimicking cascade delivery could trap drugs at the tumor site with deep penetration, high accumulation, and long-term retention.

3.6. *In vivo* antitumor efficacy and biological safety

The *in vivo* antitumor efficacy of the different formulations was evaluated in nude mice bearing subcutaneous HepG2 tumors (Fig. 6A).

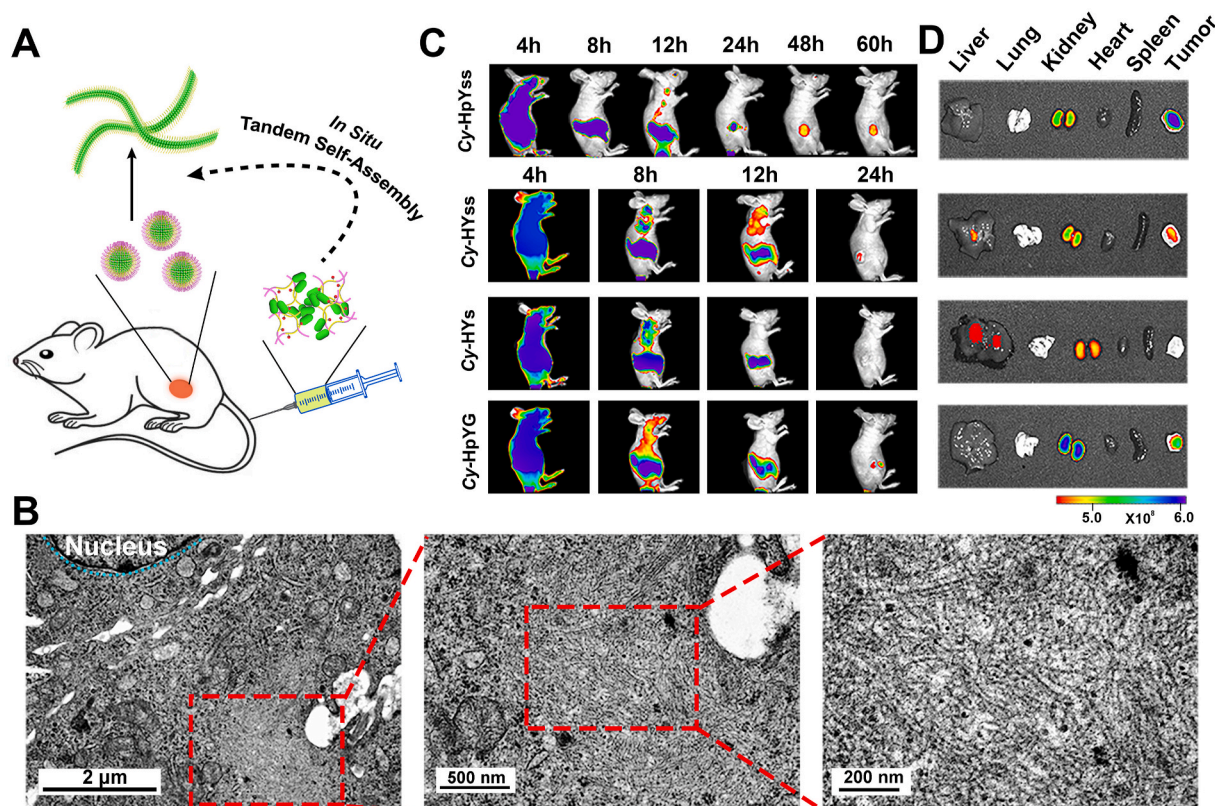


Fig. 5. *In vivo* and *ex vivo* biodistribution analysis of organelle-mimicking nanomedicine by *in situ* self-assembly in the subcutaneous tumor model. (A) Scheme of *in situ* conversion of oligomers-nanoparticles-nanofibers by tandem self-assembly after intravenous injection. (B) Bio-TEM images of ultrathin sections of excised tumor tissues at 12 h post-administration of **HpYss** (3 mg/mL); the cyan dashed line represents the nucleus boundary; scale bar from left to right: 2 μm , 500 nm, 200 nm. (C) NIR fluorescent imaging of nude mice bearing HepG2 xenografts after intravenous administration of different formulations at preset time points; the injected dose was equal to 3 mg/kg HCPT. (D) *Ex vivo* fluorescence images of excised organs and tumors at 60 h for the **Cy-HpYss** group and 24 h for the others.

The nanomedicine with the concentration equal to 3 mg/kg HCPT (>1 mM) were administrated by intravenous injection. Compared to the groups of saline and free HCPT, tumor growth was remarkably suppressed by the treatment with **HpYss**, **HYss**, **HYS**, and **HpYG**. **HpYss** produced the most remarkable treatment outcome, and the tumor volume in the **HpYss**-treated group decreased to the minimum volume ($\sim 5 \text{ mm}^3$) on day 9 after three administrations. Thereafter, the tumor volume increased slightly to $\sim 20 \text{ mm}^3$ on day 30 after the termination of the experiment. However, although the tumor volumes of **HYss**-, **HYS**-, and **HpYG**-treated groups were well-controlled during the administration, they began to increase quickly after the terminated administration with final volumes of $\sim 316 \text{ mm}^3$ (**HYss**), $\sim 332 \text{ mm}^3$ (**HYS**), and $\sim 298 \text{ mm}^3$ (**HpYG**) on day 30, which was approximately 15-fold greater than that in the **HpYss**-treated group (Fig. 6B and C). From the H&E staining results in Fig. 6D, we found that more dead cells were observed in the tumor tissues after treatment with **HpYss**, **HYss**, **HYS**, and **HpYG** in comparison with the saline and free HCPT. It was worth noting that the **HpYss** group exhibited the least cellularity and significant nuclear compression and fragmentation, verifying that the organelle-mimicking cascade drug delivery system had the most potent tumor inhibition.

To assess the antitumor activity, further histological analysis was carried out in tumor tissues, including terminal deoxynucleotidyl transferase-mediated dUTP nick-end labeling (TUNEL) to evaluate apoptosis, immunofluorescence staining of anti-Ki67 for testing tumor cell proliferation, and anti-CD31 to examine angiogenesis. As expected, the most TUNEL-positive cells, the lowest expression of Ki67 and CD31 were found in the **HpYss**-treated group (Fig. 6E). Meanwhile, the quantitative fluorescence statistics showed the significant differences of these three markers between the **HpYss** group and other groups (Fig. 6F), suggesting that organelle-mimicking cascade drug delivery

could effectively inhibit tumor growth by inducing tumor cell apoptosis, controlling cell proliferation, and preventing angiogenesis in tumor tissues.

The bodyweight of mice was monitored during the treatment, and the results revealed that only the treatment with free HCPT caused obvious weight loss (Fig. 6G). H&E staining of the main organs (heart, liver, spleen, lungs, and kidneys) was conducted to evaluate the systemic toxicity of the formulations, which showed that there was no noticeable cell damage or morphological changes in the groups treated with drug-peptide formulations (**HpYss**, **HYss**, **HYS**, and **HpYG**) compared to the saline group (Fig. S26). Although renal retention was observed in Fig. 5D, the histological analysis showed that drug-peptide conjugates clearly reduced the nephrotoxicity correlated with free HCPT. The blood parameters of RBC WBC, HGB, and PLT in the model animals showed negligible *in vivo* hematotoxicity in peptide-based drug formulations. However, these blood parameters in the group treated with free HCPT deteriorated, reflecting the unavoidable side effects induced by HCPT, including thrombocytopenia, neutropenia, and anemia (Fig. S27) [48]. Meanwhile, the biochemistry analysis results demonstrated there were no evident differences in the indicators for liver damage (AST, ALT, TP, and ALB) and kidney injuries (UA, CRE, and BUN) between the saline group and other drug-peptide formulation groups, whereas the increased levels of UA, CRE, and BUN in the free HCPT group demonstrated its nephrotoxicity (Fig. S28) [49]. These observations suggest that both the precursors and prefabricated artificial organelles could significantly reduce the adverse effects of HCPT *in vivo*.

3.7. Suppression efficacy in the large-tumor model and tumor metastasis

By analyzing the growth curve of the tumor volume in Fig. 6B, we

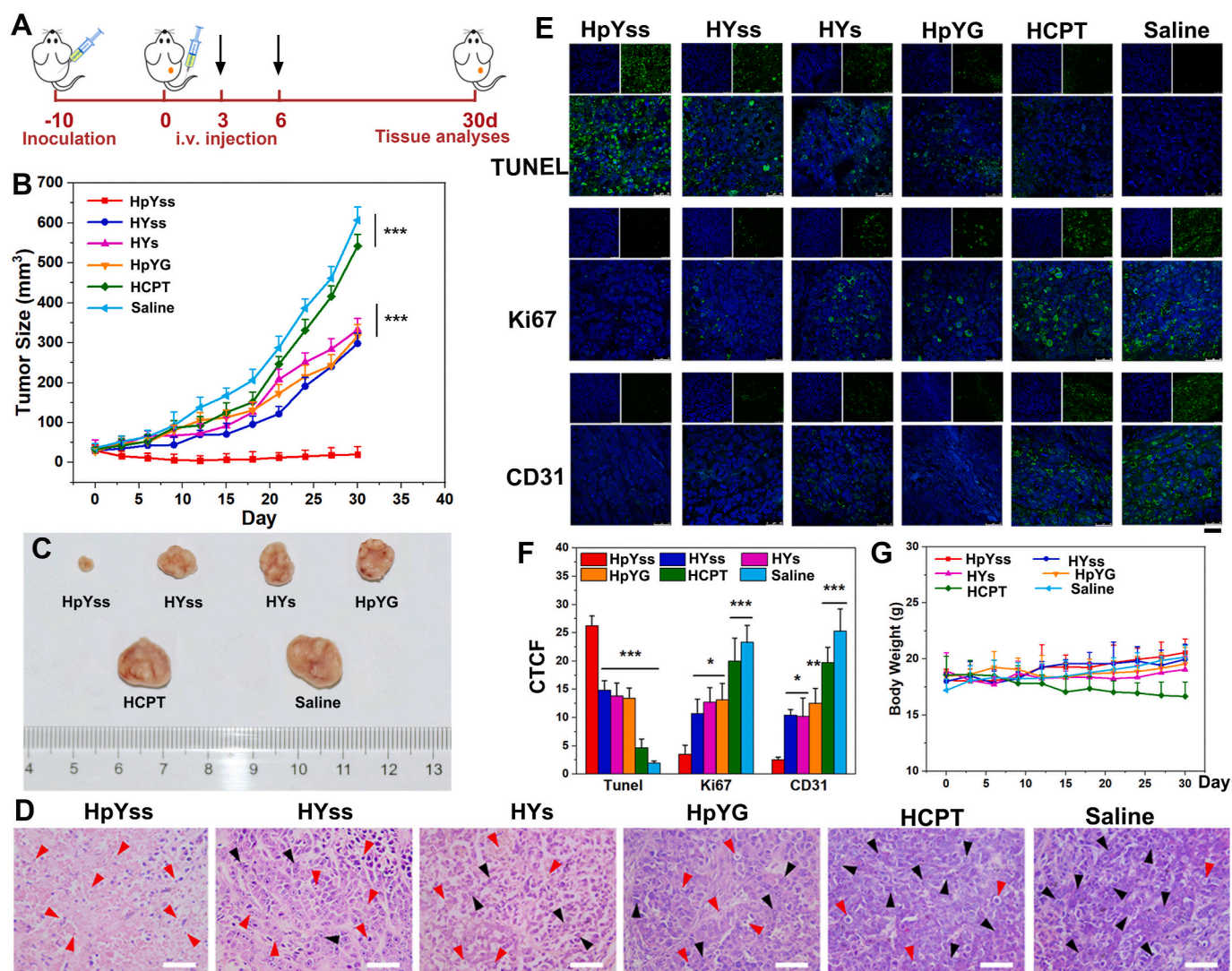


Fig. 6. *In vivo* anticancer efficacy of organelle-mimicking nanomedicine. (A) Subcutaneous HepG2 tumor growth over a 30-day period following different treatments. (B) Changes in tumor volume as a function of time in response to the indicated treatments, injected dose equal to 3 mg/kg HCPT, initial volume: 60 mm³. (C) Representative *ex vivo* photographs of tumors extracted from mice following treatments with different drug formulations; black arrows mark the proliferating cells, and red arrows indicate the apoptotic cells; scale bar: 25 μm. (D) H&E staining of tumor tissues from mice following treatments with different drug formulations; black arrows mark the proliferating cells, and red arrows indicate the apoptotic cells; scale bar: 50 μm. (E) CLSM images of tumor sections staining with TUNEL, anti-Ki67, and anti-CD31 in different treatment groups, green channel: $\lambda_{exc.} = 488$ nm, blue channel: $\lambda_{exc.} = 405$ nm for DAPI; scale bar: 25 μm. (F) The corrected total cell fluorescence (CTCF, quantified from the grayscale of the CLSM images) from tumor slices with staining of TUNEL, anti-Ki67, and anti-CD31. (G) Bodyweight changes in tumor-bearing mice corresponding to the indicated treatments. Data are presented as mean \pm SD (N = 5), * $P < 0.05$, ** $P < 0.01$, and *** $P < 0.001$ vs. **HpYss** group.

found that tumor growth was more rapid after the tumor volume reached 200 mm³, and this phenomenon was verified by the slope (K2) of the volume–time curve in the late stage, which was 4-fold higher than K1 in the early stage (Fig. S29) [50]. The increasing tumor volume substantially impaired the effectiveness of chemotherapeutics to abolish tumor growth [51]. Considering the excellent ability of **HpYss** to inhibit tumor growth, we evaluated its antitumor efficacy in a large tumor model. As shown in Fig. 7A, in a tumor model with an initial tumor volume of 300 mm³, the tumor volume decreased remarkably to \sim 103 mm³ after three administrations of **HpYss** (equal to 3 mg/kg HCPT, > 1 mM). Although an additional administration did not cause the tumor volume to continue to decrease, the tumor growth arrest was maintained, and the final tumor volume was controlled at \sim 146 mm³ (<half of the initial volume) on day 21. In comparison, the tumor volume in the saline group continued to increase to \sim 1300 mm³ at the end of the experiment (\sim 9-fold tumor volume of the **HpYss**-treated group). H&E staining revealed large areas of cellular necrosis in the tumors of mice

treated with **HpYss**, indicating the significant capacity of **HpYss** to kill tumor cells (Fig. 7B). Clear TUNEL-positive signals and negligible anti-Ki67 and anti-CD31 fluorescence signals were observed in tumor sections of the **HpYss**-treated group, demonstrating the outstanding performance of **HpYss** in inducing apoptosis and resisting tumor cell proliferation and angiogenesis (Fig. 7B and C). These results indicated that the organelle-mimicking nanomedicine produced a superior inhibitory effect on increased tumor growth.

It is well known that abundant capillary networks and sufficient circulating blood in the lungs are conducive to the invasion and retention of cancer cells [52]. Thus, liver cancer had the ability to metastasize to the lung, resulting in the rapid demise of patients [53]. The outstanding tumor-targeting effect of **HpYss** and its prominent ability to abolish tumor growth encouraged us to study its inhibitory effect on pulmonary liver cancer metastasis. Luciferase-transfected HepG2 cells (HepG2-luc) were injected into nude mice via the tail vein to construct a lung metastasis model. As shown in Fig. 7D, after 30 days, the

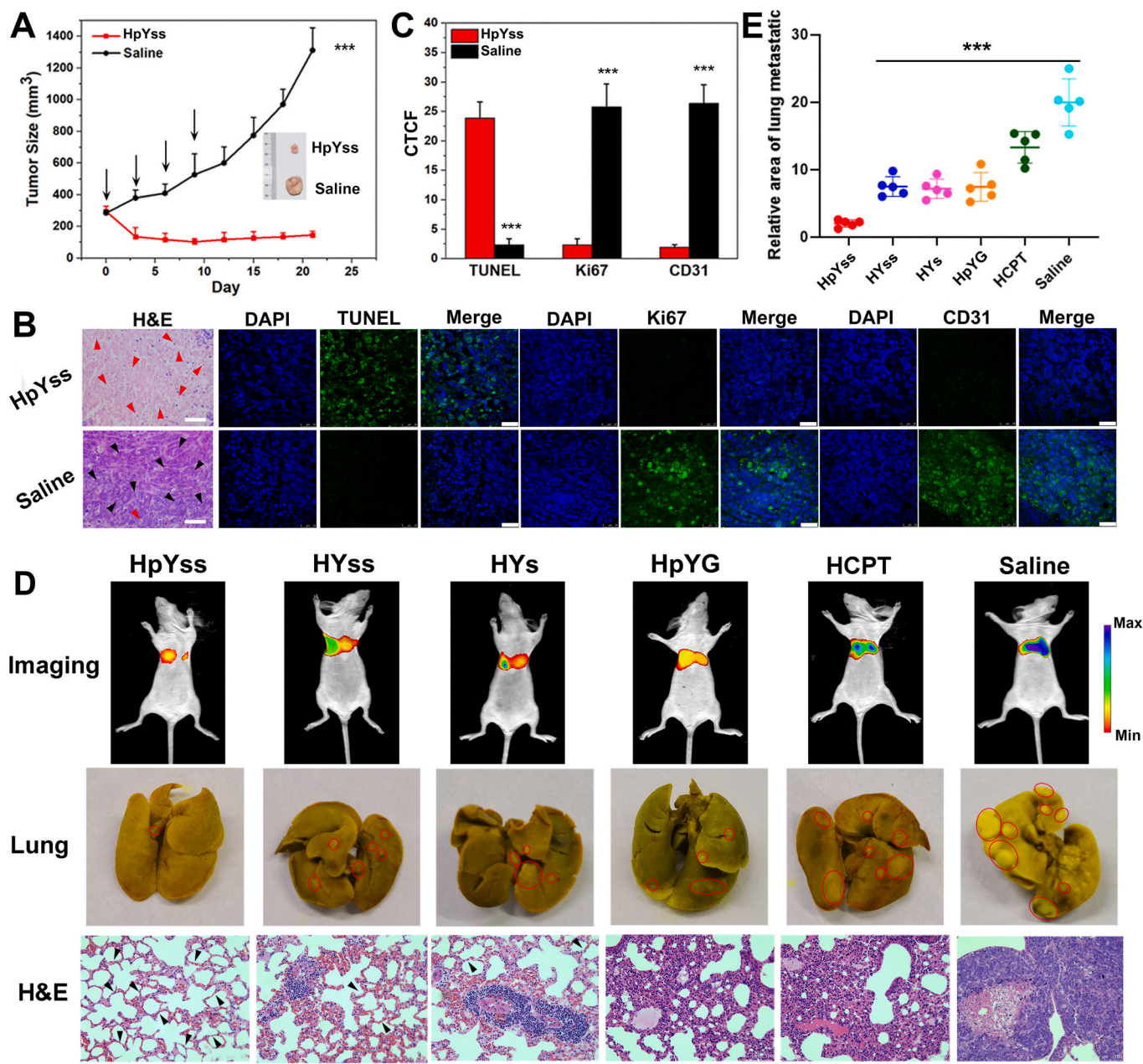


Fig. 7. *In vivo* organelle-mimicking nanomedicine suppressed tumor growth in the subcutaneous large-tumor model and lung metastasis. (A) Changes in tumor volume as a function of time treatment with **HpYss**, with an initial volume = 300 mm³, and the injected doses equal to 3 mg/kg HCPT; the inserted image shows the photographs of tumors extracted from mice on day 21. (B) H&E staining and CLSM images with TUNEL, anti-Ki67, and anti-CD31 staining of the tumor tissues from (A), scale bar of H&E staining: 50 μm, scale bar of CLSM: 25 μm; black and red arrows in the H&E staining images mark the proliferating and the apoptotic cells, respectively. (C) CTCF from tumor slices with staining of TUNEL, anti-Ki67, and anti-CD31 in (B). (D) Representative bioluminescence images (top), optical images (middle), and H&E staining images (bottom) of lung metastasis; the mice were treated with intravenous injection of different formulations at 2-day intervals after inoculation of HepG2-luci cells at day 15, and the injected dose equal to 3 mg/kg HCPT; red circles mark metastatic tumor foci, and black arrows mark normal lung tissue; scale bar: 100 μm. (E) Statistics of lung metastasis area on the surface of the excised lung tissues after treatment with different formulations. Data are presented as mean ± SD (N = 5), ***P < 0.001 vs. **HpYss** group.

bioluminescence images showed that the signal of HepG2-luci cells in the lung site of mice treated with saline and free HCPT was the strongest, whereas the signal in other groups displayed a diverse extent of decrease, indicating that the retention of cancer cells in the lung were suppressed by peptide-conjugated formulations. Unsurprisingly, the mice treated with **HpYss** exhibited an extremely substantial signal reduction in the lung, suggesting the highest efficacy of **HpYss** in ameliorating cancer cells to invade the lung. The lowest number of pulmonary metastatic nodules was also observed in the excised lung

tissues of mice administered with **HpYss**, and H&E staining of lung sections further verified a healthy tissue morphology with minimal damage in this group (Fig. 7D and E). These observations confirmed the potency of organelle-mimicking nanomedicine in preventing lung metastasis of liver cancer.

4. Conclusions

Simulating controllable and dynamic self-assembly in biological

systems to obtain functional nanostructures for drug delivery, matter exchange, and gene regulation has long attracted the keen interest of researchers and provided rich inspiration for the biomimetic construction of nanomaterials [54,55]. In this study, we presented an organelle-mimicking nanomedicine **HpYss** with the property of morphological transformation from nanoparticles to nanofibers. Through an experimental phase diagram, we elucidated the influence of A&G contents on the self-assembled nanostructures. In addition, CLSM and bio-TEM results verified that the expressed ALP and GSH of HepG2 cells could drive **HpYss** to *in situ* form nano-assemblies with a dynamic transformation from nanoparticles (**arti-EVs**) to nanofibers (**arti-Filams**), thereby promoting nuclear delivery. According to the experimental and rational analysis, we infer that the size-shape transformation from **arti-EVs** (~50–100 nm) to **arti-Filams** (4–9 nm) is of key importance to organelle-mimicking nanomedicines achieving cascade delivery of extracellular-to-intracellular-to-nucleus. **HpYss** selectively exhibits significant nuclear accumulation and, in turn, enhances the cytotoxicity of HCPT in HepG2 cells. In addition, the tunability of **HpYss** in size and shape by *in situ* self-assembly endows it with deep penetration, high accumulation, and long-term retention in solid tumors, achieving outstanding suppression of tumor growth and pulmonary metastasis *in vivo*. In essence, our innovative strategy designs an organelle-mimicking drug delivery system for self-adaptive nanomedicine in response to the milieu of HepG2 cells for precise subcellular molecular transport, which may unlock new avenues for the development of revolutionary nanotherapeutics for significantly enhanced chemotherapeutic efficiency in cancer treatment.

CRedit authorship contribution statement

Jie Zhan: Methodology, Investigation, Validation, Formal analysis, Writing – original draft, Writing – review & editing, Funding acquisition. **Yuhan Wang:** Methodology, Investigation, Validation. **Shaodan Ma:** Investigation, Validation. **Qin Qin:** Investigation, Validation. **Ling Wang:** Formal analysis, Data curation. **Yanbin Cai:** Conceptualization, Formal analysis, Writing – original draft, Writing – review & editing, Supervision, Funding acquisition. **Zhimou Yang:** Conceptualization, Resources, Project administration, Supervision, Funding acquisition.

Declaration of competing interest

The authors declare that they have no known competing financial interests or personal relationships that could have appeared to influence the work reported in this paper.

Acknowledgments

We thank Prof. Chihua Fang from Zhujiang hospital of Southern Medical University for sharing the HepG2-luci cells and the c(RGDfC) peptide. We acknowledge the financial support from the National Science Fund for Distinguished Young Scholars (31825012), National Natural Science Foundation of China (21875116, 31961143004, 81921004, 31900952, 51973090), Tianjin Science Fund for Distinguished Young Scholars (17JJCJC44900), Guangdong Basic and Applied Basic Research Foundation (2018A030313446, 2019A1515011706, 2019A1515110638), and the China Postdoctoral Science Foundation (BX20190149, 2019M662972).

Appendix B. Supplementary data

Supplementary data to this article can be found online at <https://doi.org/10.1016/j.bioactmat.2021.07.021>.

References

- [1] P. Hollenbeck, Organelle transport: moving in different directions, *Nature* 319 (1986) 724–725.
- [2] D.M. Pegtel, S.J. Gould, Exosomes, *Annu. Rev. Biochem.* 88 (2019) 487–514.
- [3] P. Li, S. Banjade, H. Cheng, S. Kim, B. Chen, L. Guo, M. Llaguno, J. V. Hollingsworth, D.S. King, S.F. Banani, P.S. Russo, Q. Jiang, B.T. Nixon, M. K. Rosen, Phase transitions in the assembly of multivalent signalling proteins, *Nature* 483 (2012) 336–340.
- [4] A. Wada, M. Fukuda, M. Mishima, E. Nishida, Nuclear export of actin: a novel mechanism regulating the subcellular localization of a major cytoskeletal protein, *EMBO J.* 17 (1998) 1635–1641.
- [5] J. Dopic, K. Skarp, E. Kaisa Rajakylä, K. Tanhuanpää, M.K. Vartiainen, Active maintenance of nuclear actin by importin 9 supports transcription, *Proc. Natl. Acad. Sci. U.S.A.* 109 (2012) E544.
- [6] J. Marine, S. Dawson, M.A. Dawson, Non-genetic mechanisms of therapeutic resistance in cancer, *Nat. Rev. Canc.* 20 (2020) 743–756.
- [7] N. Gong, N.C. Sheppard, M.M. Billingsley, C.H. June, M.J. Mitchell, Nanomaterials for T-cell cancer immunotherapy, *Nat. Nanotechnol.* 16 (2021) 25–36.
- [8] M.J. Mitchell, M.M. Billingsley, R.M. Haley, M.E. Wechsler, N.A. Peppas, R. Langer, Engineering precision nanoparticles for drug delivery, *Nat. Rev. Drug Discov.* 20 (2021) 101–124.
- [9] J. Mu, J. Lin, P. Huang, X. Chen, Development of endogenous enzyme-responsive nanomaterials for theranostics, *Chem. Soc. Rev.* 47 (2018) 5554–5573.
- [10] Q. Sun, Z. Zhou, N. Qiu, Y. Shen, Rational design of cancer nanomedicine: nanoproperty integration and synchronization, *Adv. Mater.* 29 (2017) 1606628.
- [11] L. Pan, J. Liu, J. Shi, Cancer cell nucleus-targeting nanocomposites for advanced tumor therapeutics, *Chem. Soc. Rev.* 47 (2018) 6930–6946.
- [12] X. Guo, X. Wei, Y. Jing, S. Zhou, Size changeable nanocarriers with nuclear targeting for effectively overcoming multidrug resistance in cancer therapy, *Adv. Mater.* 27 (2015) 6450–6456.
- [13] G. Cheng, J. Perez-Mercader, Dissipative self-assembly of dynamic multicompartimentalized microsystems with light-responsive behaviors, *Inside Chem.* 6 (2020) 1160–1171.
- [14] Y. Lin, Y. Wang, H. An, B. Qi, J. Wang, L. Wang, J. Shi, L. Mei, H. Wang, Peptide-based autophagic gene and cisplatin Co-delivery systems enable improved chemotherapy resistance, *Nano Lett.* 19 (2019) 2968–2978.
- [15] R.W. Chakroun, A. Sneider, C.F. Anderson, F. Wang, P. Wu, D. Wirtz, H. Cui, Supramolecular design of unsymmetric reverse bolaamphiphiles for cell-sensitive hydrogel degradation and drug release, *Angew. Chem. Int. Ed.* 59 (2020) 4434–4442.
- [16] L. Yang, R. Peltier, M. Zhang, D. Song, H. Huang, G. Chen, Y. Chen, F. Zhou, Q. Hao, L. Bian, M. He, Z. Wang, Y. Hu, H. Sun, Desuccinylation-triggered peptide self-assembly: live cell imaging of SIRT5 activity and mitochondrial activity modulation, *J. Am. Chem. Soc.* 142 (2020) 18150–18159.
- [17] J. Zhou, X. Du, C. Berciu, H. He, J. Shi, D. Nicastro, B. Xu, Enzyme-instructed self-assembly for spatiotemporal profiling of the activities of alkaline phosphatases on live cells, *Inside Chem.* 1 (2016) 246–263.
- [18] X. Dou, C. Feng, Amino acids and peptide-based supramolecular hydrogels for three-dimensional cell culture, *Adv. Mater.* 29 (2017) 1604062.
- [19] C.H. Chen, L.C. Palmer, S.I. Stupp, Self-repair of structure and bioactivity in a supramolecular nanostructure, *Nano Lett.* 18 (2018) 6832–6841.
- [20] F. Sainsbury, Emergence by design in self-assembling protein shells, *ACS Nano* 14 (2020) 2565–2568.
- [21] A. Buchberger, C.R. Simmons, N.E. Fahmi, R. Freeman, N. Stephanopoulos, Hierarchical assembly of nucleic acid/coiled-coil peptide nanostructures, *J. Am. Chem. Soc.* 142 (2020) 1406–1416.
- [22] X. Liu, P. Formanek, B. Voit, D. Appelhans, Functional cellular mimics for the spatiotemporal control of multiple enzymatic cascade reactions, *Angew. Chem. Int. Ed.* 56 (2017) 16233–16238.
- [23] G. Liu, X. Wang, J. Hu, G. Zhang, S. Liu, Self-immolative polymersomes for high-efficiency triggered release and programmed enzymatic reactions, *J. Am. Chem. Soc.* 136 (2014) 7492–7497.
- [24] C.M.A. Parlett, M.A. Isaacs, S.K. Beaumont, L.M. Bingham, N.S. Hondow, K. Wilson, A.F. Lee, Spatially orthogonal chemical functionalization of a hierarchical pore network for catalytic cascade reactions, *Nat. Mater.* 15 (2016) 178–182.
- [25] J. Zhan, Y. Cai, S. He, L. Wang, Z. Yang, Tandem molecular self-assembly in liver cancer cells, *Angew. Chem. Int. Ed.* 57 (2018) 1813–1816.
- [26] Z. Feng, H. Wang, S. Wang, Q. Zhang, X. Zhang, A.A. Rodal, B. Xu, Enzymatic assemblies disrupt the membrane and target endoplasmic reticulum for selective cancer cell death, *J. Am. Chem. Soc.* 140 (2018) 9566–9573.
- [27] F. Zhang, G. Zhu, O. Jacobson, Y. Liu, K. Chen, G. Yu, Q. Ni, J. Fan, Z. Yang, F. Xu, X. Fu, Z. Wang, Y. Ma, G. Niu, X. Zhao, X. Chen, Transformative nanomedicine of an amphiphilic camptothecin prodrug for long circulation and high tumor uptake in cancer therapy, *ACS Nano* 11 (2017) 8838–8848.
- [28] R. Dominguez, K.C. Holmes, Actin structure and function, *Annu Rev Biophys* 40 (2011) 169–186.
- [29] L. Blanchoin, R. Boujemaa-Paterski, C. Sykes, J. Plastino, Actin dynamics, architecture, and mechanics in cell motility, *Physiol. Rev.* 94 (2014) 235–263.
- [30] A.G. Cheetham, P. Zhang, Y. Lin, L.L. Lock, H. Cui, Supramolecular nanostructures formed by anticancer drug assembly, *J. Am. Chem. Soc.* 135 (2013) 2907–2910.
- [31] Z. Feng, H. Wang, R. Zhou, J. Li, B. Xu, Enzyme-instructed assembly and disassembly processes for targeting downregulation in cancer cells, *J. Am. Chem. Soc.* 139 (2017) 3950–3953.

- [32] M.H. Lee, E. Kim, H. Lee, H.M. Kim, M.J. Chang, S.Y. Park, K.S. Hong, J.S. Kim, J. L. Sessler, Liposomal texaphyrin theranostics for metastatic liver cancer, *J. Am. Chem. Soc.* 138 (2016) 16380–16387.
- [33] Z. Feng, H. Wang, F. Wang, Y. Oh, C. Berciu, Q. Cui, E.H. Egelman, B. Xu, Artificial intracellular filaments, *Cell Rep. Phys. Sci.* 1 (2020) 100085.
- [34] Z. Dong, L. Feng, Y. Chao, Y. Hao, M. Chen, F. Gong, X. Han, R. Zhang, L. Cheng, Z. Liu, Amplification of tumor oxidative stresses with liposomal fenton catalyst and glutathione inhibitor for enhanced cancer chemotherapy and radiotherapy, *Nano Lett.* 19 (2019) 805–815.
- [35] L.A. Mulcahy, R.C. Pink, D.R.F. Carter, Routes and mechanisms of extracellular vesicle uptake, *J. Extracell. Vesicles* 3 (2014) 24641.
- [36] A. Xie, S. Hanif, J. Ouyang, Z. Tang, N. Kong, N.Y. Kim, B. Qi, D. Patel, B. Shi, W. Tao, Stimuli-responsive prodrug-based cancer nanomedicine, *Ebiomedicine* 56 (2020) 102821.
- [37] X. Ling, J. Tu, J. Wang, A. Shajii, N. Kong, C. Feng, Y. Zhang, M. Yu, T. Xie, Z. Bharwani, B.M. Aljaeid, B. Shi, W. Tao, O.C. Farokhzad, Glutathione-responsive prodrug nanoparticles for effective drug delivery and cancer therapy, *ACS Nano* 13 (2019) 357–370.
- [38] P.L. Paine, L.C. Moore, S.B. Horowitz, Nuclear envelope permeability, *Nature* 254 (1975) 109–114.
- [39] S. Huo, S. Jin, X. Ma, X. Xue, K. Yang, A. Kumar, P.C. Wang, J. Zhang, Z. Hu, X. Liang, Ultrasmall gold nanoparticles as carriers for nucleus-based gene therapy due to size-dependent nuclear entry, *ACS Nano* 8 (2014) 5852–5862.
- [40] E. Hinde, K. Thammasiraphop, H.T.T. Duong, J. Yeow, B. Karagoz, C. Boyer, J. J. Gooding, K. Gaus, Pair correlation microscopy reveals the role of nanoparticle shape in intracellular transport and site of drug release, *Nat. Nanotechnol.* 12 (2017) 81–89.
- [41] E. Blanco, H. Shen, M. Ferrari, Principles of nanoparticle design for overcoming biological barriers to drug delivery, *Nat. Biotechnol.* 33 (2015) 941–951.
- [42] H. Li, J. Du, X. Du, C. Xu, C. Sun, H. Wang, Z. Cao, X. Yang, Y. Zhu, S. Nie, J. Wang, Stimuli-responsive clustered nanoparticles for improved tumor penetration and therapeutic efficacy, *Proc. Natl. Acad. Sci. U.S.A.* 113 (2016) 4164.
- [43] J. Wang, W. Mao, L.L. Lock, J. Tang, M. Sui, W. Sun, H. Cui, D. Xu, Y. Shen, The role of micelle size in tumor accumulation, penetration, and treatment, *ACS Nano* 9 (2015) 7195–7206.
- [44] B. Kim, G. Han, B.J. Toley, C. Kim, V.M. Rotello, N.S. Forbes, Tuning payload delivery in tumour cylindroids using gold nanoparticles, *Nat. Nanotechnol.* 5 (2010) 465–472.
- [45] H. An, L. Li, Y. Wang, Z. Wang, D. Hou, Y. Lin, S. Qiao, M. Wang, C. Yang, Y. Cong, Y. Ma, X. Zhao, Q. Cai, W. Chen, C. Lu, W. Xu, H. Wang, Y. Zhao, A tumour-selective cascade activatable self-detained system for drug delivery and cancer imaging, *Nat. Commun.* 10 (2019) 4861.
- [46] Y. Zhong, J. Zhan, G. Xu, Y. Chen, Q. Qin, X. Liao, S. Ma, Z. Yang, Y. Cai, Enzyme-instructed self-assembly enabled monomer–excimer transition to construct higher ordered luminescent supramolecular assembly for activity-based bioimaging, *Angew. Chem. Int. Ed.* 60 (2021) 8121–8129.
- [47] Q. Li, S. Li, S. He, W. Chen, P. Cheng, Y. Zhang, Q. Miao, K. Pu, An activatable polymeric reporter for near-infrared fluorescent and photoacoustic imaging of invasive cancer, *Angew. Chem. Int. Ed.* 59 (2020) 7018–7023.
- [48] X. Xu, Y. Cheng, J. Wu, H. Cheng, S. Cheng, R. Zhuo, X. Zhang, Smart and hyperfast responsive polyprodrug nanopatform for targeted cancer therapy, *Biomaterials* 76 (2016) 238–249.
- [49] J. Li, W. Xu, D. Li, T. Liu, Y.S. Zhang, J. Ding, X. Chen, Locally deployable nanofiber patch for sequential drug delivery in treatment of primary and advanced orthotopic hepatomas, *ACS Nano* 12 (2018) 6685–6699.
- [50] W.L. Corwin, H. Ebrahimi-Nik, S.M. Floyd, P. Tavousi, I.I. Mandoiu, P. K. Srivastava, Tumor Control Index as a new tool to assess tumor growth in experimental animals, *J. Immunol. Methods* 445 (2017) 71–76.
- [51] J. West, P.K. Newton, Chemotherapeutic dose scheduling based on tumor growth rates provides a case for low-dose metronomic high-entropy therapies, *Canc. Res.* 77 (2017) 6717.
- [52] N.K. Altorki, G.J. Markowitz, D. Gao, J.L. Port, A. Saxena, B. Stiles, T. McGraw, V. Mittal, The lung microenvironment: an important regulator of tumour growth and metastasis, *Nat. Rev. Canc.* 19 (2019) 9–31.
- [53] C.L. Chaffer, R.A. Weinberg, A perspective on cancer cell metastasis, *Science* 331 (2011) 1559.
- [54] X. Ji, L. Ge, C. Liu, Z. Tang, Y. Xiao, W. Chen, Z. Lei, W. Gao, S. Blake, D. De, B. Shi, X. Zeng, N. Kong, X. Zhang, W. Tao, Capturing functional two-dimensional nanosheets from sandwich-structure vermiculite for cancer theranostics, *Nat. Commun.* 12 (2021) 1124.
- [55] N. Kong, W. Tao, X. Ling, J. Wang, Y. Xiao, S. Shi, X. Ji, A. Shajii, S.T. Gan, N. Y. Kim, D.G. Duda, T. Xie, O.C. Farokhzad, J. Shi, Synthetic mRNA nanoparticle-mediated restoration of p53 tumor suppressor sensitizes p53-deficient cancers to mTOR inhibition, *Sci. Transl. Med.* 11 (2019) w1565.